Backshell Radiative Heating on Human-Scale Mars Entry Vehicles

Thomas K. West IV* John E. Theisinger†
Andrew J. Brune‡ and Christopher O. Johnston§
NASA Langley Research Center, Hampton, VA 23681

This work quantifies the backshell radiative heating experienced by payloads on human-scale vehicles entering the Martian atmosphere. Three underlying configurations were studied: a generic sphere, a sphere-cone forebody with a cylindrical payload, and an ellipsled. Computational fluid dynamics simulations of the flow field and radiation were performed using the LAURA and HARA codes, respectively. Results of this work indicated the primary contributor to radiative heating is emission from the CO_2 IR band system. Furthermore, the backshell radiation component of heating can persist lower than 2 km/s during entry and descent. For the sphere-cone configuration a peak heat flux of about 3.5 W/cm^2 was observed at the payload juncture during entry. At similar conditions, the ellipsled geometry experienced about 1.25 W/cm^2 on the backshell, but as much as 8 W/cm^2 on the base at very high angle of attack. Overall, this study sheds light on the potential magnitudes of backshell radiative heating that various configurations may experience. These results may serve as a starting point for thermal protection system design or configuration changes necessary to accommodate thermal radiation levels.

Nomenclature

D	Diameter	T_{tr}	Translational Temperature
I	Intensity	T_v	Vibrational-Electronic Temperature
q_r	Radiative Heat Flux	V	Velocity
q_λ	Monochromatic Heat Flux	ρ	Density

I. Introduction

During entry into the Martian atmosphere, vehicles are subject to a challenging aerothermodynamic environment. A significant amount of work has gone into characterizing both convective and radiative heating on the forebody of entry vehicles.[1–4] The primarily CO_2 Mars atmosphere presents different issues than Earth's atmosphere, particularly with regards to radiation. One particular area of interest is the afterbody region. As the hot gases from the forebody shock-layer spill into the afterbody region, they can establish a large volume of gas that can radiate onto the backshell of the vehicle. For Earth entry, this radiation, and even forebody radiation, is typically only an issue for super-orbital velocity entries.[5] At Mars, however, radiation can be an issue at speeds well below orbital speed.

In previous missions to Mars, the radiative heating environment in the afterbody region was neglected during thermal protection system (TPS) design due to the expectation of minimal contribution and lack of accurate wake environment modeling capabilities. Informed by additional experimental testing,[6] CO_2 infrared (IR) emission is now known to be a significant contributor to radiative heating. This is of particular interest to vehicles traveling well below orbital speed where the CO_2 molecule is not dissociated, but rather

*Aerospace Engineer, Vehicle Analysis Branch, Systems Analysis and Concepts Directorate, Member AIAA.
†Aerospace Engineer, Atmospheric Flight and Entry Systems Branch, Engineering Directorate, Member AIAA.
‡Aerospace Engineer, Structural and Thermal Systems Branch, Engineering Directorate, Member AIAA.
§Aerospace Engineer, Aerothermodyanmics Branch, Research Directorate, Member AIAA.

is highly vibrationally excited. Work by Brandis et al.[7] showed the potential impact of radiation from the wake flow onto the backshell as a result of CO_2 IR radiation on multiple capsule like geometries, including the Mars Science Lab configuration. However, this work was done on smaller, robotic-scale vehicles. As NASA progresses closer to the human exploration of Mars, significantly larger vehicles will likely be used to land both crew and cargo onto the surface. To effectively protect from the radiative environment that may be experienced, the potential heating on the backshell of such human-scale entry vehicles needs to be quantified.

The primary objective of this work is to quantify the backshell radiative heating that payloads on human-scale vehicles entering the Martian atmosphere may experience. The goal will be to investigate three underlying configurations: a generic sphere, a sphere-cone forebody with a cylindrical payload, and an ellipsled. The sphere geometry serves as a fundamental case study and is used to identify key features and trends of backshell radiation. The other two configurations are representative of designs currently being investigated by NASA. The goal will be to determine the dependency of the radiation on different geometries and to quantify the magnitude of the radiative heating in the backshell region of each configuration. This information can be used to size appropriate thermal protection systems for future missions.

The next section details the computational models used in the radiative heating analysis. Section III presents the sphere study. Sections IV and V present the results of the sphere-cone with a cylindrical payload and ellipsled studies, respectively. The last section summarizes this work and details the key findings.

II. Computational Models

In this study, the flow field was modeled using the LAURA finite-volume, Navier-Stokes flow solver.[8] This solver uses a second-order, upwind, discretization scheme with Roe's flux-difference splitting scheme and Yee's Symmetric Total Variation Diminishing (STVD) formulation of the inviscid flux. For all cases, the flow field was assumed to be steady state with a two-temperature, thermochemical nonequilibrium model.[9,10] While turbulent flow is expected to develop on the forebody and extend onto the backshell of each configuration studied, the state of the boundary layer is expected to have little impact on the radiative heating studied here. Furthermore, an accurate modeling of the turbulent convective heating on the backshell is beyond the scope of this study. Thus, the boundary layer was modeled as entirely laminar.

The Mars atmosphere was modeled as 97% CO_2 and 3% N_2 by mass, while the flow field was modeled using an eight species composition model: CO_2, CO, N_2, O_2, NO, C, N, O. The 11 reaction finite rate chemistry model that was used is shown in Table 1.[4] Note that the parameters in this table are those of an Arrhenius form, and the equation for the forward reaction rate is given by Eq. (1). Backward reaction rates are computed assuming quasi-steady state.

Table 1: Uncertain Flowfield Chemical Kinetics

#	Reaction	$A_{f,i}$	$n_{f,i}$	$D_{f,i}$	$T_{f,i}$	Ref.
1	$CO_2 + M \leftrightarrow CO + O + M$	1.38e+22	−1.50	6.328e+4	T_a	N, C, O
		6.90e+21	−1.50	6.328e+4	T_a	others
2	$CO + M \leftrightarrow C + O + M$	1.20e+21	−1.00	1.29e+5	T_a	N, C, O
		1.80e+21	−1.00	1.29e+5	T_a	others
3	$N_2 + M \leftrightarrow 2N + M$	3.00e+22	−1.60	1.132e+5	T_a	N, C, O
		7.00e+21	−1.60	1.132e+5	T_a	others
4	$NO + M \leftrightarrow N + O + M$	4.40e+17	0.00	7.55e+4	T_a	N, C, O, NO, CO_2
		2.00e+15	0.00	7.55e+4	T_a	others
5	$O_2 + M \leftrightarrow 2O + M$	1.00e+22	−1.50	5.936e+04	T_a	N, C, O
		2.00e+21	−1.50	5.936e+04	T_a	others
6	$CO_2 + O \leftrightarrow O_2 + CO$	2.71e+14	0.0	3.38e+4	T_{tr}	
7	$CO + NO \leftrightarrow CO_2 + N$	3.00e+06	0.88	1.33e+4	T_{tr}	
8	$CO + O \leftrightarrow O_2 + C$	3.90e+13	−0.18	6.92e+4	T_{tr}	
9	$N + CO \leftrightarrow NO + C$	1.10e+14	0.07	5.35e+4	T_{tr}	
10	$N_2 + O \leftrightarrow NO + N$	6.00e+13	0.1	3.80e+4	T_{tr}	
11	$O_2 + N \leftrightarrow NO + O$	2.49e+09	1.18	4.01e+3	T_{tr}	

$$k_{f,i} = A_{f,i} T_{f,i}^{n_{f,i}} exp(-D_{f,i}/T_{f,i}) \tag{1}$$

The entire surface of each configuration was assumed to be non-ablating and in radiative equilibrium with a fully-catalytic to homogeneous recombination wall boundary condition. Note that the wall catalyst model on a non-ablating surface has a negligible effect on the surface radiative heating.[3]

The radiation was modeled using the High-Temperature Aerothermodynamic Radiation (HARA) code.[11,12] In the present study, the flow field solver and the radiative heat transfer calculations are loosely coupled. Note that the radiating gas in the afterbody region can become increasingly optically thick.[7] A line-by-line treatment of the CO_2 and CO molecules is used rather than a smeared rotational band model to ensure accuracy.

The HARA code uses a tangent-slab approximation for computing the radiative flux and its divergence; however, Brandis et al.[7] showed that the tangent-slab approximation can cause the radiation to be overpredicted in the afterbody region. A full ray-tracing or angular integration approach[16] is necessary to produce accurate predictions of the radiation. All results shown in this work applied the HARA ray-tracing approach to compute radiative heating.

III. Sphere Geometry

As a preliminary study of the backshell radiation, the first geometry studied was a sphere. Spheres with three diameters were investigated: 2, 10, and 20 meters. These diameters are in the range of possible aeroshell or entry vehicle scales needed for large payload delivery to the Martian surface. These spheres were studied at velocities of 2, 3, 4, and 5 km/s and at densities of 10^{-4} and 10^{-3} kg/m^3. This range covers the conditions a vehicle may traverse during planetary entry and descent. The goal was to use results from a more fundamental geometry to inform the analysis of more complex shapes studied later. Also, the use of a simple geometry may eventually allow for the development of engineering relationships for use in analysis and design.

A. Radiation Mechanisms

Before analyzing the results as a whole, a discussion of the radiation features is necessary to inform the results and trends that will be shown for the suite of cases. As a sample case for this, the 20 m sphere at 3.0 km/s and 10^{-3} kg/m^3 was studied. Later this case is shown to be extreme in terms of the backshell radiation and is a condition that many descending vehicles may encounter. For the stagnation line, the wavelength spectrum and temperature profiles are shown in Figure 1. Notice that the primary radiation contribution is from the CO_2 IR band system. There is very minimal contribution from CO IR due to the low temperatures. The temperature profile shows that the flow is in thermodynamic equilibrium at these conditions in the stagnation region. Note the high radiation from CO_2 when the flow is between 2000 and 3000 K is in agreement with previous studies.[16]

The backshell region behaves quite similarly to the stagnation region for this and many other cases. Figure 2 shows the wavelength spectrum and temperature profiles at a selected backshell point located at about 75% of the diameter measured from the stagnation point. Notice again that the only contribution to the radiation is from the CO_2 IR band system. In the temperature profile, which is measured along the line normal to the body, there is only a small region near the wall that is just out of thermodynamic equilibrium. This would cause a slight drop in intensity, but this region is small. Otherwise the wake is primarily in thermodynamic equilibrium along this line. The important take away from this is that CO_2 is the primary emitter at these conditions. Even for the higher speed studied here, there is not enough energy in the flow to strongly excite CO,[3] even though CO is present due to CO_2 dissociation. This is discussed later in this section.

B. Analysis and Results

Figure 3 shows a summary of the sphere results. There are several important features and trends that can be observed as a function of all three varied parameters. First, the diameter dependency is as expected. The radiation to the surface increases proportionally to the sphere diameter due to a stronger shock and thicker shock-layer (i.e., more excited CO_2). This is true both in the forebody and on the backshell. Note that the increase is not linear with the diameter becasuse CO_2 IR is not optically thin. What is possibly not so intuitive is that the maximum radiation does not always occur at the stagnation point. Notice at the higher velocities that peak radiative heating occurs downstream of the stagnation point, but still on the forebody.

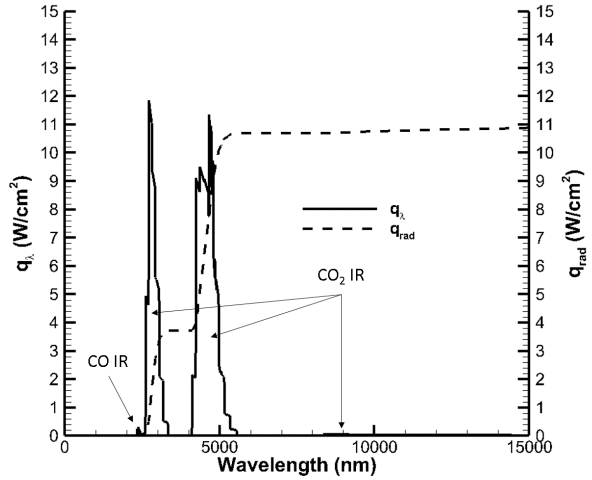

(a) Monochromatic and cumulative flux spectrum.

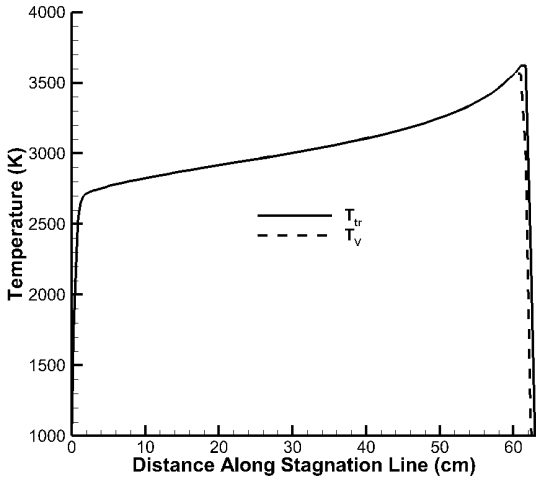

(b) Temperature.

Figure 1: Stagnation line radiative flux and temperature profile. D = 20 m, V = 3.0 km/s and ρ = 0.001 kg/m^3.

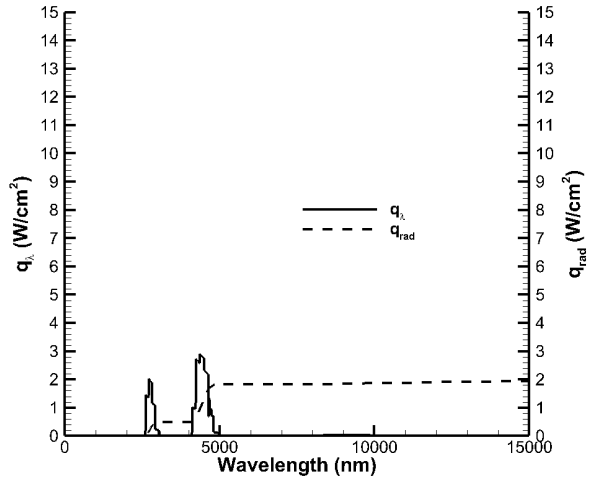

(a) Monochromatic and cumulative flux spectrum.

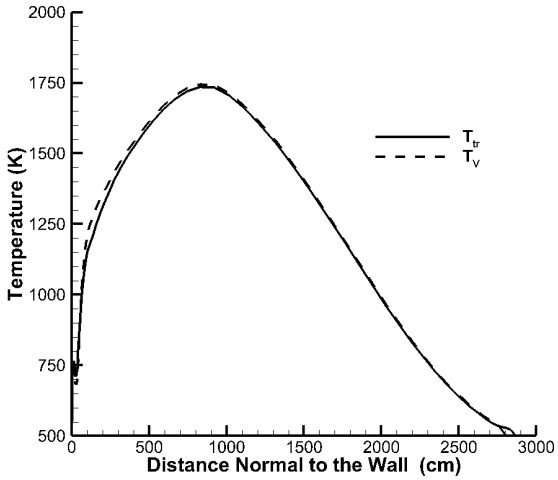

(b) Temperature.

Figure 2: Backshell radiative flux and temperature profile. D = 20 m, V = 3.0 km/s and ρ = 0.001 kg/m^3.

This again is related to the strength of the shock. At lower velocities, the shock is just strong enough to excite the CO_2 molecule resulting in emission from the IR band. At velocities above about 3 km/s, the higher temperatures produced behind the shock results in dissociation of CO_2 to CO. However, for a fixed temperature and number density, the CO IR band is a weaker emitter than the CO_2 IR band. This results in the observed lower radiative heating at the stagnation point. Downstream, there is more undissociated, but excited CO_2 resulting in higher radiation at the surface.

Moving along the surface to the backshell region (x/D > 0.5), radiative heating decreases to some nonzero value for all cases. This is significant because, even when the surface normal is aligned with the flow direction (i.e., on the backshell), there is still radiation to the surface. For the 20 m diameter sphere, the radiative heating can be greater than 5 W/cm^2, which emanates from two primary sources. The first is as excited

flow from the forebody expands into the backshell region, it radiates to the body. The second source is the recompression region in the wake. There is a significant, local temperature rise in this region that causes emission from CO_2. This is shown in the temperature contour in Figure 4 for the 20 m sphere at 3 km/s and 0.001 kg/m^3. This figure also illustrates where in the flow the radiation is coming from at a point on the backshell. The hemisphere on the surface of the sphere geometry shows that a portion of the radiation emanates from the forebody region, but there is also a large contribution from the recompression area. For the more complex geometries discussed later, these features will hold true, but the main point is that the radiation is significant in the backshell region even for velocities as low as 2 km/s and that the source of radiation is not just the gas near the forebody. The results shown here will be revisited for comparison to those observed for the more complex geometries.

C. Convergence

For backshell radiation analyses, there are three components of convergence measure: grid resolution, wake distance, and the number of rays used in the ray tracing approach. For the 20 m diameter sphere at 3.0 km/s and 0.001 kg/m^3, a summary of the impact that these convergence measures have on the radiation at a selected point on the backshell is shown in Table 2. Notice that for each of these components the maximum change from the baseline radiation prediction is less than 2%. Doubling the grid resolution normal to the surface has the least impact. Extending the wake distance beyond the baseline five diameters makes little impact. This result is in agreement with Brandis et al.[7] who observed a four diameter wake was necessary for the Mars Science Lab capsule configuration. The number of rays used in the ray tracing also has little impact, even for 100 times more rays. Overall, the results of these convergence tests for sphere cases may be used to inform the analysis of more complex shapes; however, a word of caution should be noted. The baseline values for the sphere should be considered the minimums needed for other analyses. As with any CFD study, grids are geometry dependent.

Table 2: Comparison of convergence measures on predicted backshell radiation.

Measure	Baseline	Improvement	% Difference
Normal Grid Density	125	250	1.18
Wake Distance (Diameters)	5	8	1.24
Number of Rays (each body point)	265	22500	1.79

D. Uncertainty Analysis

The simplicity of the sphere cases also allows for a quick look at the uncertainty and sensitivities in radiation predictions on the backshell. Previous work has investigated the impact of various sources of uncertainty only in the forebody and for speeds greater than 6.0 km/s.[2,3,17] At the lower speeds studied here and in the backshell region, there is not significant emission or absorption from any of the CO band systems. This greatly reduces the potential sources of input uncertainty to those that only impact CO_2 radiation. In this work, three sources of uncertainty were considered and are shown in Table 3. Note that all of these sources are assumed to be epistemic as there is not significant evidence to support any probability distribution claim.

Table 3: Sources of uncertainty.

Source	Uncertainty	Ref.
CO_2 + M $\leftrightarrow$ CO + O + M Forward Rate	-1, +0 om	3
CO_2 IR Oscillator Strength	$\pm$ 30%	3
CO IR Oscillator Strength	$\pm$ 30%	3

The point collocation, non-intrusive polynomial chaos method was used to efficiently and accurately propagate the uncertainty. This approach has been used extensively in many aerospace applications and, more

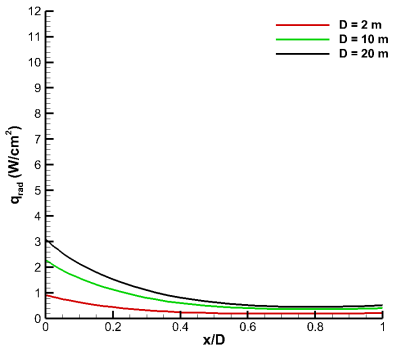

(a) V = 2.0 km/s, $\rho = 10^{-3}$.

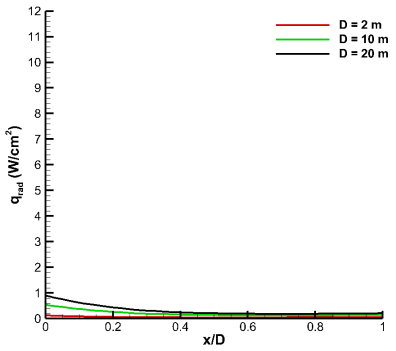

(b) V = 2.0 km/s, $\rho = 10^{-4}$.

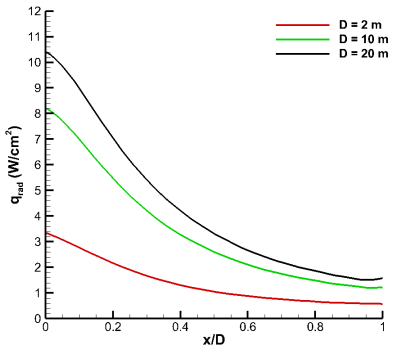

(c) V = 3.0 km/s, $\rho = 10^{-3}$.

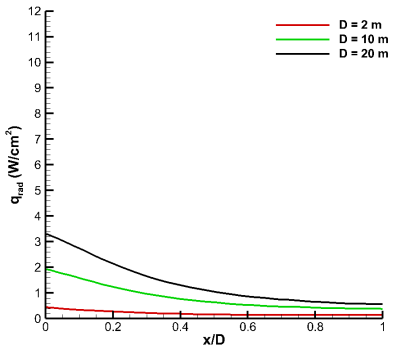

(d) V = 3.0 km/s, $\rho = 10^{-4}$.

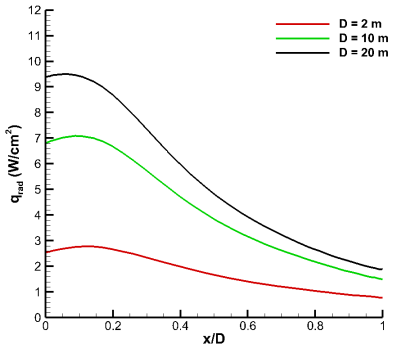

(e) V = 4.0 km/s, $\rho = 10^{-3}$.

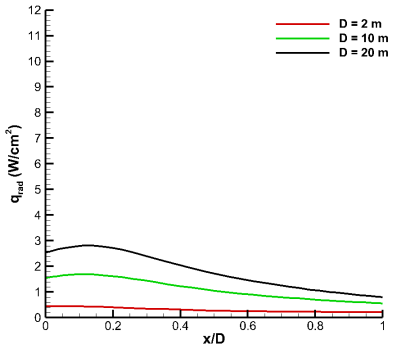

(f) V = 4.0 km/s, $\rho = 10^{-4}$.

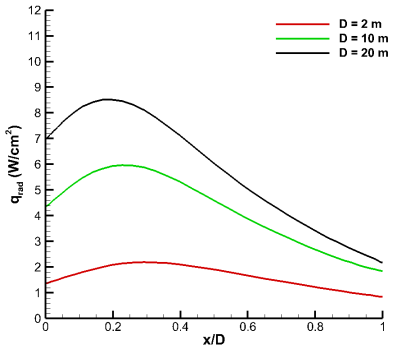

(g) V = 5.0 km/s, $\rho = 10^{-3}$.

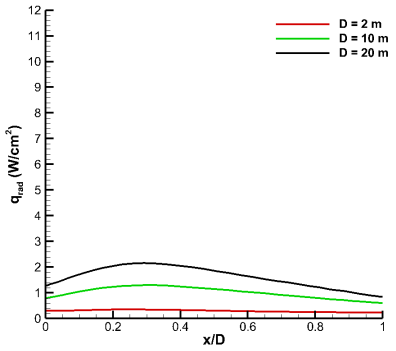

(h) V = 5.0 km/s, $\rho = 10^{-4}$.

Figure 3: Radiation along a sphere.

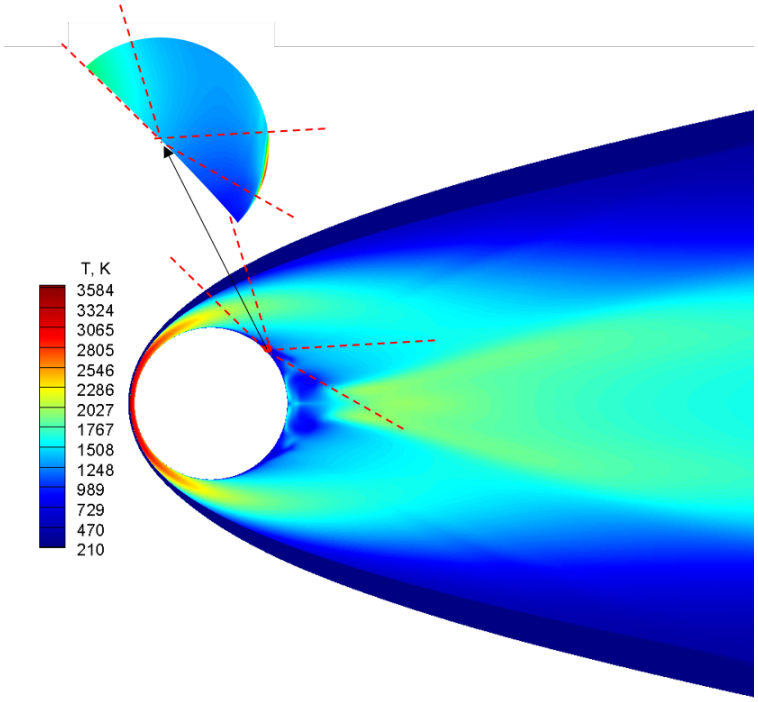

Figure 4: Contour of translational temperature. D = 20 m, V = 3.0 km/s and ρ = 0.001 kg/m^3.

particularly in radiation prediction uncertainty analyses.[2,17,20] Additionally, polynomial chaos expansions can be used to compute the Sobol indices used to determine the contribution of each parameter to the total uncertainty.[21] Further details of both approaches are left to the references.[18,19]

Figure 5 shows the results of the uncertainty analysis for a 20 m sphere at a speed of 3.0 km/s and density of 10^{-3} kg/m^3. At the stagnation point, the uncertainty can range from 10% below the nominal to more than 30% over the nominal. This is the widest variation along the sphere surface. In the backshell region, the radiation varies from about -6% to over 20% above the nominal prediction. More interestingly, the variation in the sensitivity along the sphere depicts differences from the stagnation point. In this region, the dissociation of CO_2 is the more important uncertainty source, which is expected given that this is where the dissociation occurs. Downstream, the CO_2 IR oscillator strength becomes the more significant source of uncertainty, until reaching the backshell region; however the CO_2 dissociation rate is a factor as there may still be some dissociation, as well as recombination that is impacted by this uncertainty. In the afterbody, the CO_2 rate becomes the dominate contributor to the uncertainty again due to recombination of any dissociated CO_2.

IV. Sphere-cone with Cylindrical Payload

This section presents the afterbody radiative heating results for a sphere-cone with cylindrical payload. This configuration is a representative geometry similar to proposed hypersonic inflatable aerodynamic decelerator (HIAD) vehicle concepts.[16,22] Compared to previous rigid aeroshells, the inflatable concept offers a combination of increased payload mass to the surface and high-altitude deceleration. One of the technical challenges of the HIAD is the radiative heating in the afterbody region of the vehicle. This section investigates, in particular, the potential radiative heating on the cylindrical payload and backshell, as well as the effects of the flow characteristics on this heating for a range of freestream conditions.

A 16 m sphere-cone with a 8 m blunted spherical nose and 70-deg half-angle cone is considered as the heatshield of a human-scale vehicle entering the Martian atmosphere. The cylindrical body is attached to the backshell of the heatshield and represents the payload with a diameter of 7.2 meters. The entire body, including the payload and heat shield, is considered to be rigid. Figure 6 shows a schematic of this geometry.

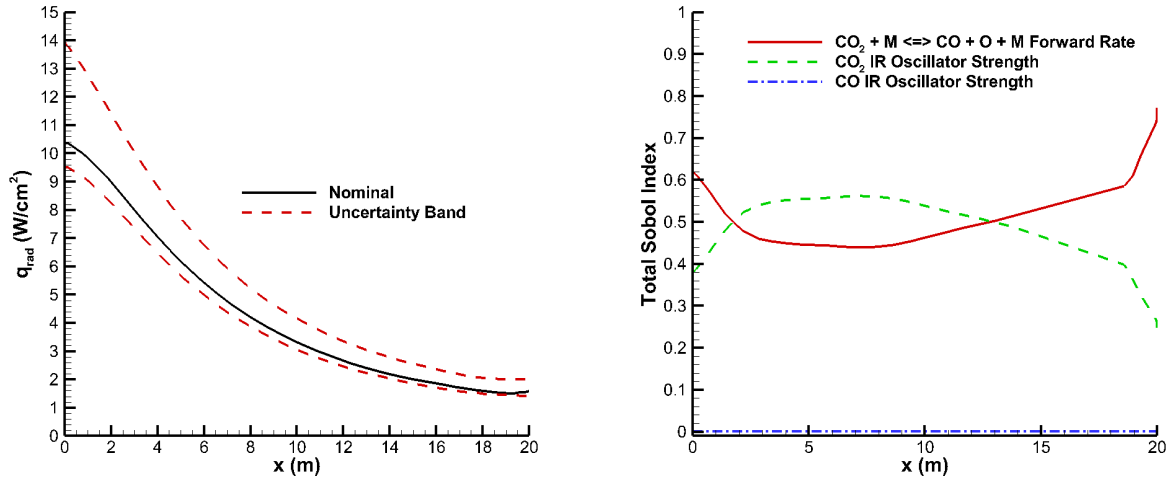

(a) Uncertainty band.

(b) Sensitivity distribution.

Figure 5: Uncertainty band and sensitivity distribution along the sphere. D = 20 m, V = 3.0 km/s and $\rho = 10^{-3}$ kg/m^3.

Note that the bridging juncture between the backshell and payload has a smooth and variable incline surface rather than a conventional sharp corner.

A structured grid with 192 blocks surrounds half of the sphere-cone and payload surfaces with a symmetry plane located at the centerline. For each block, 106 surface normal grid cells emanate from the surface. The grid extends six body lengths into the wake, downstream of the aft most point of the payload. Results indicate consistently that the afterbody radiation for wake distances of four and six body lengths are identical to within 1% for a sample of the cases presented in this section. This is similar to the convergence study shown for the spheres.

The forebody and afterbody flow is considered for a set of trajectory points during aerocapture and entry phases to study potential radiative heating on the backshell and payload. Table 4 presents the freestream conditions and orientation of the vehicle for the selected aerocapture and entry trajectory points. In the next two subsections, the afterbody radiative heating results are presented and compared for the aerocapture and entry trajectories. For both trajectory phases, the peak radiative heat flux on the afterbody is identified, and the contributing ray intensity distributions to the radiative flux are shown and discussed at the corresponding surface points. The contributions of the dominate molecular band systems are also analyzed. With the range of freestream conditions considered, conclusions are made on the relationship of the afterbody radiative heat flux to the flow characteristics and forebody radiative heat flux.

A. Aerocapture

This subsection examines the afterbody radiative heating environment for the aerocapture trajectory. Peak radiative heating of about 1.5 W/cm^2 occurs at the 175s trajectory point. Figure 7 presents the afterbody radiative flux distribution within a 14m-diameter circle of influence, which includes the backshell and payload surfaces. A sample of 547 afterbody surface points in this region were computed with ray-tracing and interpolated on the surface grid. Each surface point requires the radiative intensity along 360 lines of sight. This is representative of all cases presented in this section. The maximum afterbody radiative flux is located at the juncture on the centerline and on the leeward side (top portion) of the surface for all cases, which are summarized later. The windward (bottom) region of the afterbody surface has, in general, lower radiative fluxes compared to the leeward region. The reason for the higher radiative heating on the leeward portion of the afterbody can be explained with Figures 8 and 9. Because the vehicle is oriented at an angle of attack, the CO_2 molecule is more dissociated within the forebody shock layer on the windward side compared to the leeward side. On the leeward side, more undissociated, vibrationally-excited CO_2, flows from the forebody to the afterbody.

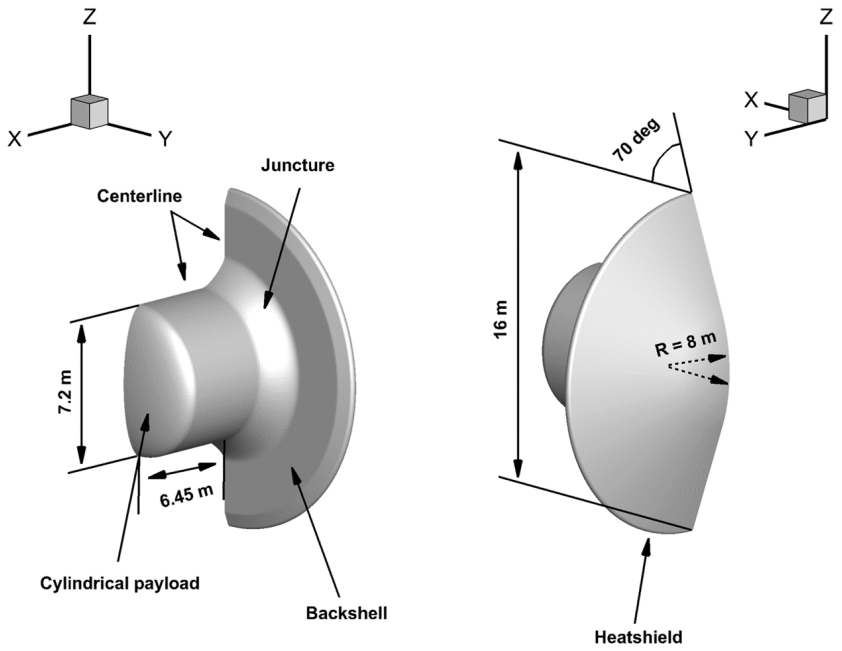

Figure 6: Geometry of the sphere-cone with cylindrical payload.

Table 4: Reference freestream conditions and vehicle orientation for the sphere-cone aerocapture and entry trajectories.

Traj. Phase	Time (s)	α (deg)	β (deg)	V_∞ (m/s)	ρ_∞ (kg/m^3)	T_∞ (K)
Aerocapture	75	9.5	0.0	6233	5.20e-6	144
	125	9.5	0.0	6075	7.64e-5	152
	150	9.5	0.0	5796	1.33e-4	154
	175	9.5	0.0	5466	1.39e-4	155
	250	9.5	0.0	4876	4.72e-5	147
Entry	100	6.0	0.0	4739	3.03e-5	139
	120	6.0	0.0	4650	1.18e-4	130
	140	6.0	0.0	4390	2.86e-4	154
	150	6.0	0.0	3938	5.23e-4	173
	192	6.0	0.0	3025	9.04e-4	188
	210	6.0	0.0	2565	1.07e-3	193
	230	6.0	0.0	2142	1.25e-3	197

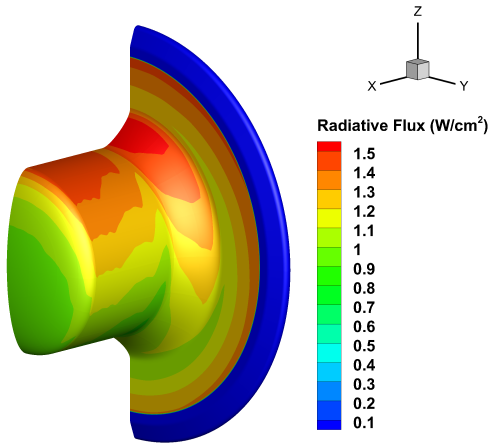

Figure 7: Radiative flux distribution on the afterbody at 175 s.

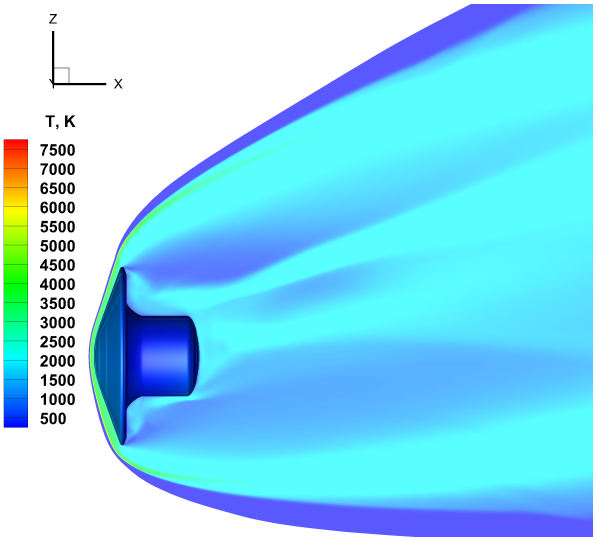

Figure 8: Vibrational temperature flow contour along the symmetry plane at 175 s.

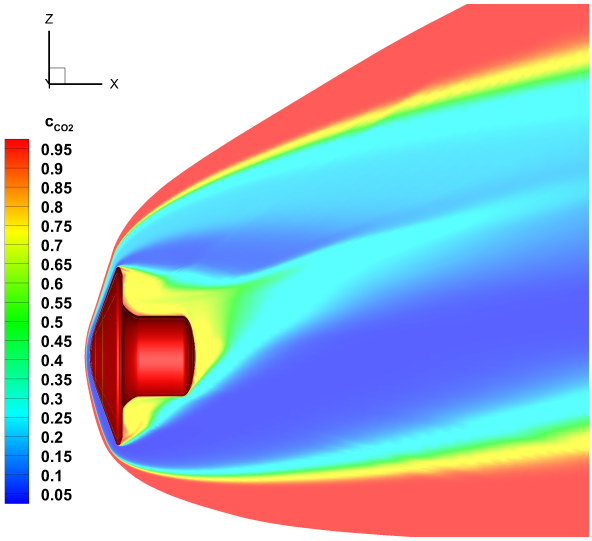

Figure 9: CO_2 mass fraction flow contour along the symmetry plane at 175 s.

The results in Figure 7 also show that there is an additional peak in the radiative flux on the top and aft portion of the payload. The peak at the payload is comparable but slightly lower than the maximum radiative flux at the juncture. Figure 10 presents the radiant intensity angular distribution on a projected hemisphere, oriented normal to the peak juncture and payload body points. Reference hemispherical rays that intersect the surface points and the outer grid boundary are shown for correspondence between the radiant intensity angular distributions and the afterbody flow. The origin of each radiant intensity contours in Figure 10 coincides with the body normal vector. The integrated heat flux is calculated by integrating the radiant intensity over the surface area of the hemisphere plot with respect to the solid angle. The results show the asymmetric distribution of the radiant intensity, which explains why the afterbody radiation must be computed with ray tracing as opposed to tangent slab approximation. The radiant intensities are, however, symmetric about the symmetry plane, which explains the peak radiative fluxes at the centerline.

The angular distribution plots further show that the maximum radiant intensities are centered on the rays that pass through a region of highly-concentrated CO_2 gas at high vibrational temperatures of about 3000 K in the afterbody flow. For example, the strongest intensities for the juncture in Figure 10(a) correspond to the afterbody flow region, downstream of the shoulder, with much higher CO_2 mass fractions compared to the

forebody. At high velocities above 5 km/s during aerocapture, the forebody vibrational temperatures are too high near the shoulder and cause significant dissociation of CO_2. In Figure 10(b), the results are consistent with the juncture body point and show the same flow region for which strongest intensities originate. There is also a stream of CO_2 gas downstream of the aft most point of the payload which contributes a focal point of intensity on the right of each body point hemisphere plot. These results are in agreement with previous studies by Mazaheri[16] and Brandis et al.,[7] which show that the relatively low temperatures between 2000 and 3000 K in the shock layer and afterbody flow resulting in strongly emitting CO_2 molecules to remain undissociated at mid-infrared wavelengths.

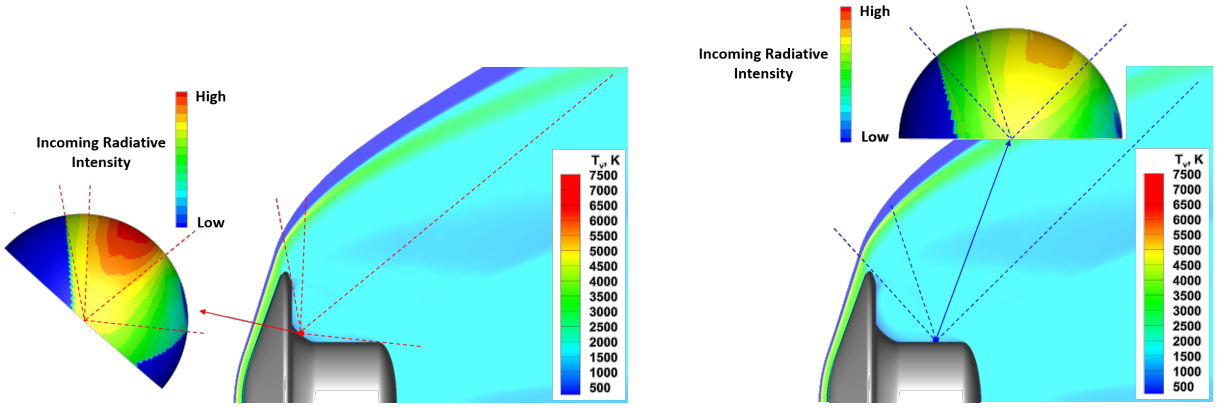

(a) Juncture. (b) Payload.

Figure 10: Radiant intensity distribution projected on hemisphere normal to the peak flux body points at 175 s.

The impact of CO_2 emission on the radiative flux for the juncture body point is presented in Figure 11(c). The CO_2 IR molecular band system provides the dominant backshell radiation component throughout the aerocapture trajectory. Other than the CO_2 IR band system, the CO IR band emission provides a noticeable contribution to the backshell radiation at velocities greater than 5 km/s, as a result of more dissociated CO gas flowing into the afterbody wake. Comparing this result to the forebody, the CO 4th Positive and CO IR bands become more significant to the radiation near the stagnation point and leeward shoulder in Figures 11(a) and 11(b), respectively. There is a noticeable transition from the dominating CO 4th Positive band at higher velocities near 75 seconds to the dominating CO_2 IR at lower velocities near 250 seconds at the stagnation point. Between these strong spectrum emissions, the CO IR band becomes a significant contributor. At lower temperatures away from the stagnation point, around the shoulder and in the backshell, the expected result of decreased CO emission is seen. This provides a strong argument for the presence of strongly emitting CO_2 molecules, which results in increased radiation near the shoulder and around the afterbody.

A summary of the radiative heating magnitudes for the aerocapture trajectory at the peak forebody and afterbody surface points are detailed in Figure 12. As expected, the peak radiative flux on the forebody occurs on the shoulder based on the previous discussion regarding increased presence of CO_2 at these velocities below 7 km/s. The results show the afterbody radiative flux is significant compared to the peak forebody radiative flux, and in some cases above 6 km/s, can reach comparable levels. Furthermore, the maximum radiative heat loads for the shoulder and juncture were estimated to be 265 and 190 J/cm^2, respectively. Even though the afterbody radiative heat load may seem low but significant relative to the forebody, the magnitude is important for the design of a TPS on the backshell and payload, considering there is additional heat load from the entry trajectory.

B. Entry

This subsection examines the afterbody radiative heating environment for the entry trajectory phase. Compared to aerocapture, the vehicle during entry is exposed to flow at higher densities and lower velocities and flies at a smaller angle of attack, which could potentially have dramatic effects on the afterbody radiation. Figure 13 presents the afterbody radiative flux throughout the entry trajectory for designated body points on the backshell and payload surfaces. The radiative fluxes have at least tripled in magnitude relative to

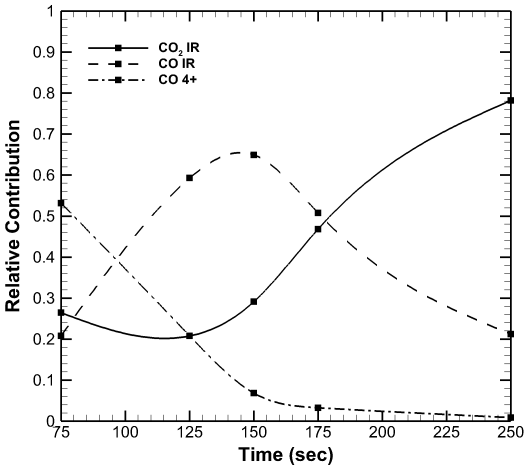

(a) Stagnation Point

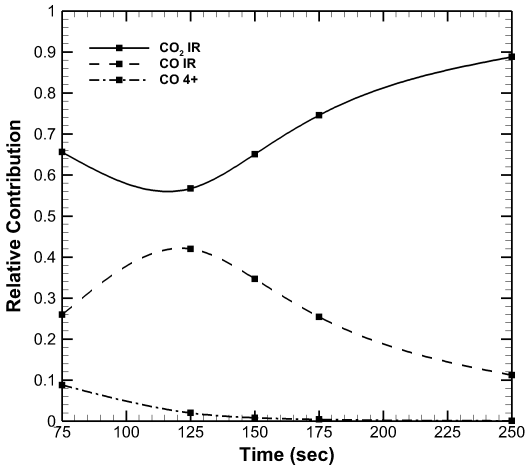

(b) Shoulder.

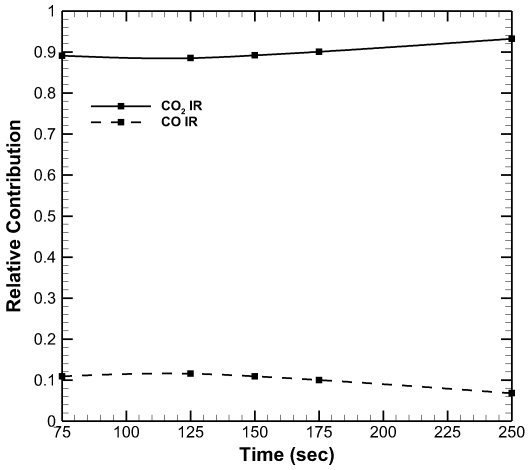

(c) Juncture.

Figure 11: Molecular band spectrum contributions to the total radiative flux at various body points for aerocapture.

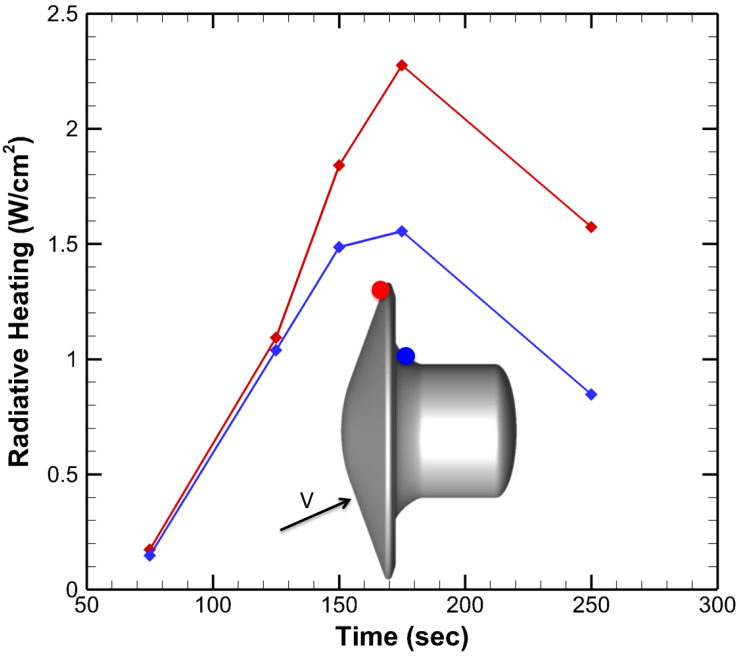

Figure 12: Peak radiation on the forebody and afterbody for aerocapture.

aerocapture, which can be explained by increased presence of CO_2 at lower velocities. Peak radiative heating of about 3.6 W/cm^2 occurs at the 192 s trajectory point, followed by a decrease in radiative heating at later times. The decrease in radiative flux later in the trajectory can be explained by the reduced temperatures within the shock layer at velocities below 3 km/s. The results in Figure 13 also show that the payload surface near the body axis on the leeward side experiences higher radiative fluxes for most of the trajectory, and in some cases, comparable heating to the juncture. The radiative heat load for this critical payload body point was estimated to be 310 J/cm^2. The maximum heat flux and combined heat load for both aerocapture and entry, estimated to be around 500 J/cm^2, can be significant to the design of a sensitive payload. This result can aid in the appropriate selection of TPS material and thickness requirements.

Figure 14 presents the radiative flux distribution at the 192s trajectory point for the same afterbody surface region as in the previous subsection. The same number of lines of sight and body points were used to produce these results as in the aerocapture case presented in Figure 7. Compared to the aerocapture case, the peak radiative flux is now located on the payload centerline on the leeward side instead of the juncture. An additional peak, similar to aerocapture, is also located on the juncture centerline on the leeward side. Because the vehicle is oriented at an angle of attack, the windward region of the afterbody surface has lower radiative fluxes compared to the leeward region due to dissociation of CO_2 in the shock layer. This is consistent with results seen for aerocapture. Figures 15 and 16 show that the leeward flowfield region with high vibrational temperatures and high CO_2 mass fraction radiates strongest and produces magnified radiative fluxes on the leeward payload and juncture surfaces. Comparing Figure 16 to Figure 9, much higher concentrations of CO2 exist in the afterbody flowfield for this entry condition than for the aerocapture condition.

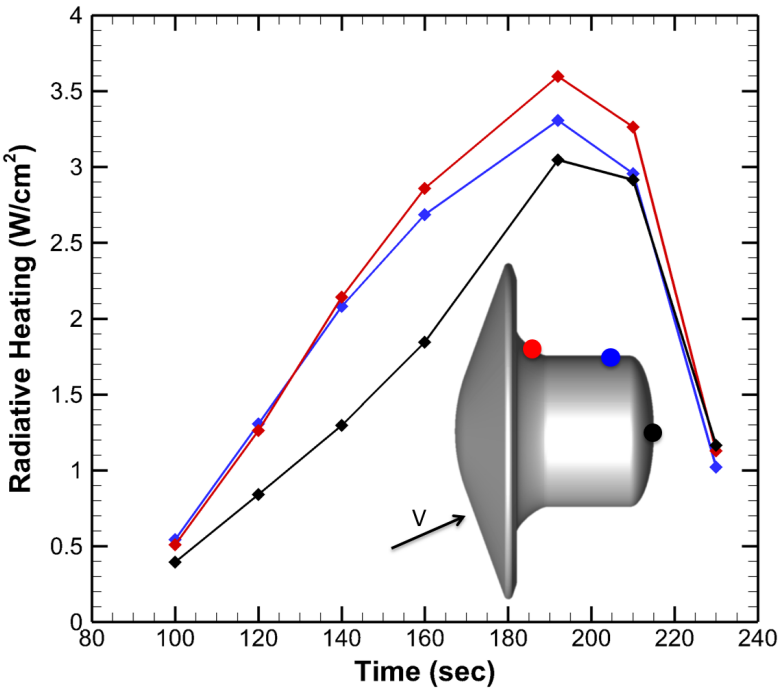

Figure 13: Afterbody radiation throughout the entry trajectory.

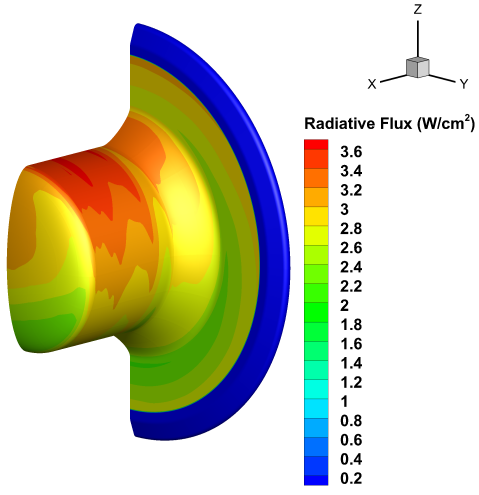

Figure 14: Radiative flux distribution on the afterbody at 192 s

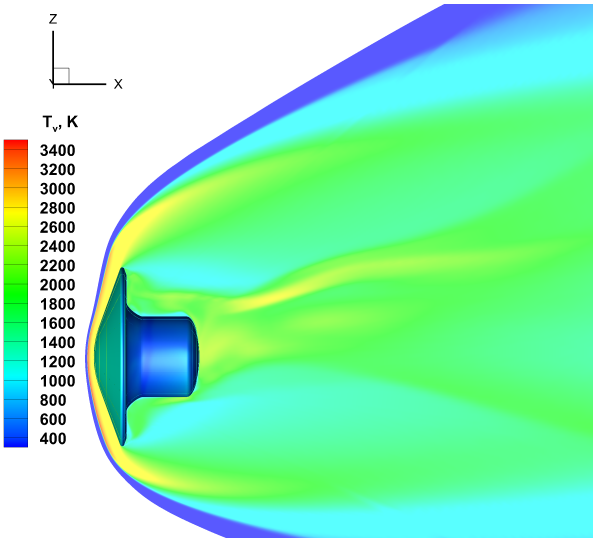

Figure 15: Vibrational temperature flow contour along the symmetry plane at 192 s

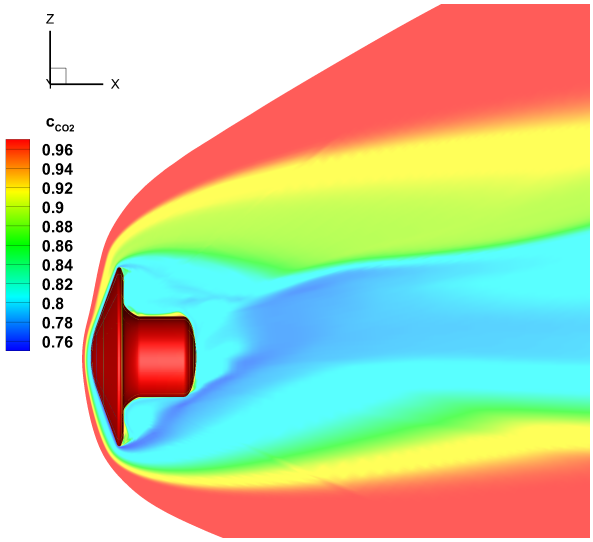

Figure 16: CO_2 mass fraction flow contour along the symmetry plane at 192 s

To investigate the flowfield regions that radiate strongest to the afterbody surface in more detail, Figure 17 presents the radiant intensity angular distributions for three body points on the backshell and payload surfaces. Reference hemispherical rays that intersect the surface points and the outer grid boundary are shown for correspondence between the radiant intensity angular distributions and the afterbody flow. The juncture and payload body points are fairly close in proximity to those presented in the previous subsection and represent the peak radiative flux locations at the symmetry plane. The aft most point of the payload is also shown for comparison to the peak body points. Figure 17(a) shows that there is negligible radiation from the surface and the recirculating flow region downstream of the payload. Comparing Figures 17(a) and 17(b), the strongest intensity comes from the flow around the shoulder, where there is a significant presence of CO_2 at high vibrational temperatures around 3000 K. The high temperature region around 3000 K shifted towards the shoulder for entry, while this vibrational temperature band extended around the shoulder and into the afterbody wake for aerocapture. Although there are slight differences in vehicle orientation between both trajectory phases, the impact of angle of attack on this flow behavior is not conclusive but could be one of the potential causes. However, it is evident that the reduced velocities below 5 km/s for entry result in lower vibrational temperatures, compared to aerocapture, near the shoulder and plays a role in the presence of undissociated CO_2 gas in the surrounding flow field. Figure 17(c) shows that the radiation is not as significant from the afterbody recirculating wake region and the high-temperature CO_2 gas near the shoulder is not visible at the aft most point of the payload. Note that the high temperature, vibrationally excited flow spilling around the shoulder expands rapidly, leading to a region of nonequilibrium that emits strongly to the surface. This same feature will be observed for the ellipsled configuration.

Comparing these results to spheres sheds light on the predictive capability of using information from the more simple geometry cases. For the sphere-cone configuration, the peak radiative heating on the backshell is about 3.5 W/cm^2. Referring back to Figure 3 to the closest point to the 192 s conditions is at the 3.0 km/s and 0.001 kg/m^3 sphere case. Using the sphere data, the backshell radiative heating ranged from about 2 to 3.5 W/cm^2. For design purposes, results from an appropriately-sized sphere may be sufficient for a preliminary estimation of the backshell heating.

V. Ellipsled Configuration

This section presents a study of the backshell radiative heat flux on an ellipsled configuration. In addition to providing an indication of radiation magnitudes, the impacts on radiation distributions due to variations in ellipsled angle of attack and length are also assessed. Results are presented for a single freestream condition that has been demonstrated to produce significant CO_2 IR radiation.

The ellipsled configuration generally consists of an elliptically-blunted nose and a cylindrical body. Such vehicles have been proposed for performing aerocapture and entry, descent, and landing (EDL) in several

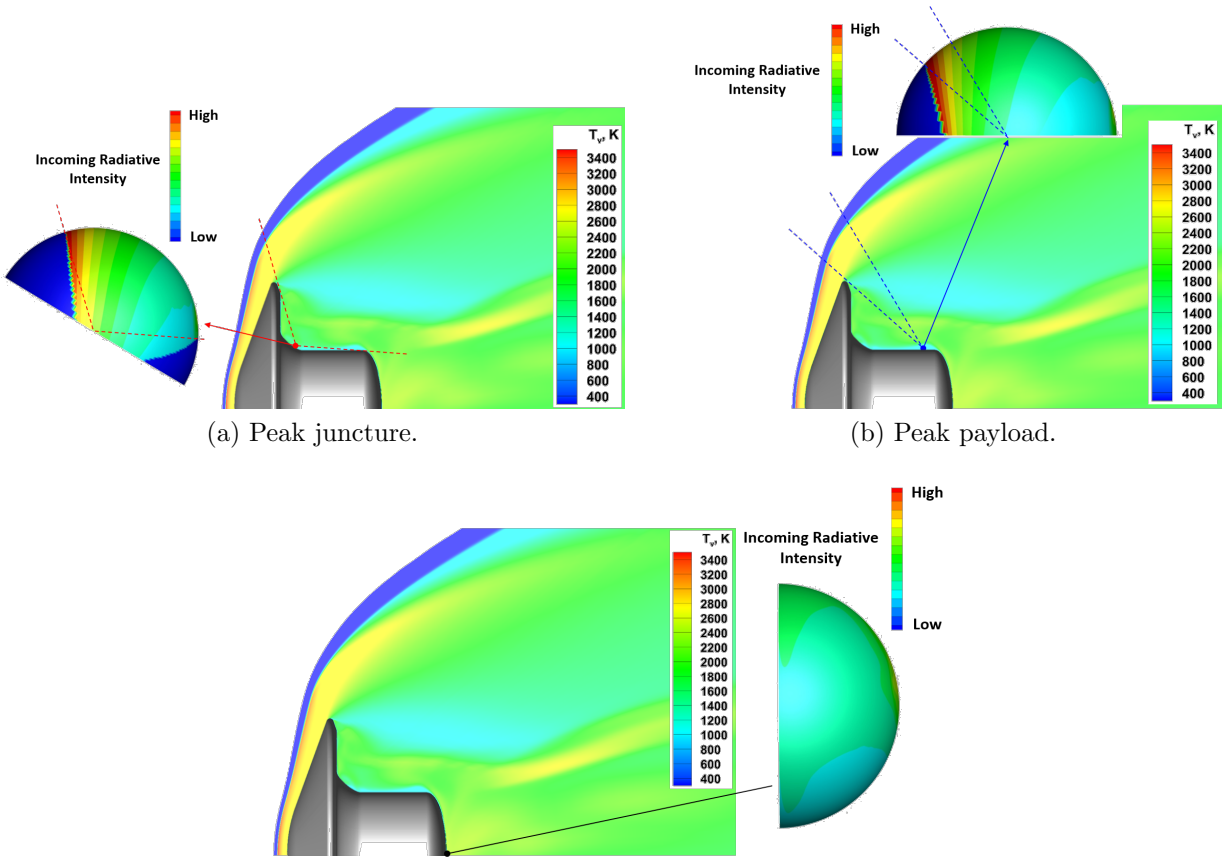

(a) Peak juncture.

(b) Peak payload.

(c) Payload aft.

Figure 17: Radiant intensity distribution projected on hemisphere normal to the various body points at 192 s.

previous human-scale Mars architecture studies.[23,24] The ellipsled configuration is appealing due to its moderately high hypersonic lift-to-drag ratio (L/D) when compared to blunt-body configurations, which places it into the "mid-L/D" class of vehicles. Such mid-L/D configurations can provide the aerodynamic performance required for sufficient deceleration and precision landing of surface assets.

The specific ellipsled configuration developed for this study is shown in Figure 18. It consists of a hemispherical nose and a cylindrical body with circular cross-section. The base corner of the body has also been designed with a finite radius. Because this study is focused on assessing human-scale vehicles, the ellipsled has been sized with an overall diameter of 10 m and a nominal total length (L) of 30 m. The base corner radius is defined to be 5% of the base radius, yielding a value of 0.25 m. To assess the impact of vehicle size on backshell radiation, ellipsled configurations with L of 20 m and 40 m were also included in this study. The backshell region of the ellipsled surface is defined as consisting of the leeside and base portions of the cylindrical body (see Figure 18).

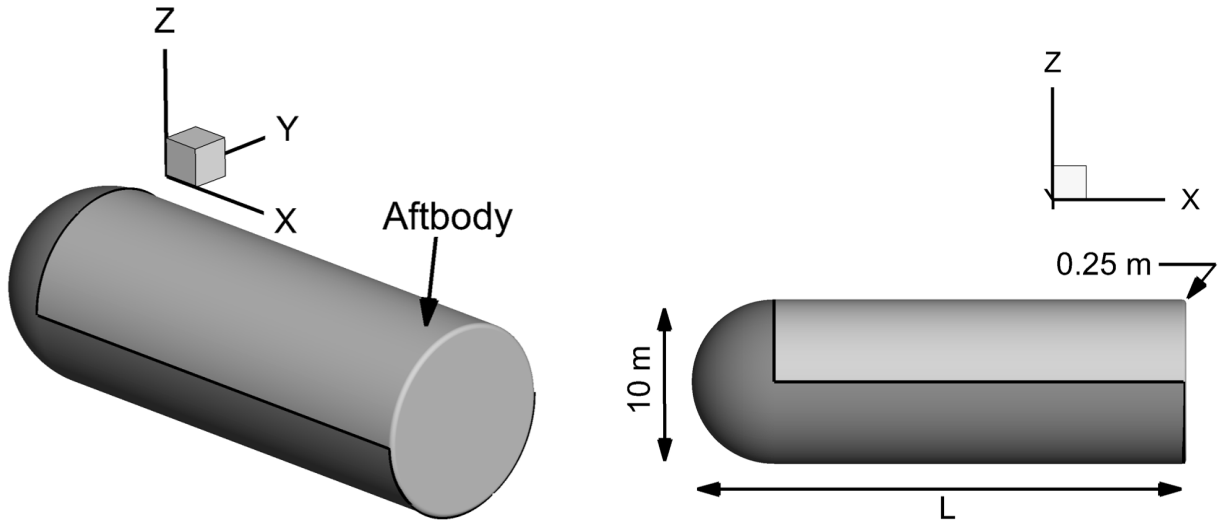

(a) Iso view. (b) Side view.

Figure 18: Ellipsled geometry with aftbody surface region highlighted.

For analysis of this ellipsled configuration, a freestream condition was sought at which CO_2 is known to be a significant emitter of IR radiation and is known to dominate the overall incident radiative heat flux. Based on the conditions explored in this work for a sphere and the entry results for the sphere-cone, a velocity 3 km/s and density of 0.001 kg/m^3 were identified as such conditions. These freestream conditions correspond to a Mach number of approximately 13 and a unit Reynolds number of approximately 3 x 10^5 m^{-1}.

The ellipsled configuration was analyzed at a nominal angle of attack of 40 deg. To assess variation in backshell radiation with varying angle of attack, the nominal (L = 30 m) ellipsled was also analyzed at 25 deg. and 55 deg. angle of attack. Such values would be similar to those employed during human-scale Mars entry and represent a variation in hypersonic L/D of approximately 0.45 to 0.6. Additionally, the sensitivity of the ellipsled length is also investigated by analyzing lengths of 20 and 40 m at the nominal 0 deg. angle of attack.

Flowfield simulations were performed using half-body grids with a symmetry boundary condition at the ellipsled centerline. The associated structured volume grids consisted of 120 blocks with 144 cells normal to the ellipsled surface. For each ellipsled configuration that was analyzed, grid adaptation was formulated such that a wake distance of at least four times the vehicle length was maintained.

A. Angle of Attack Dependency

The L = 30 m ellipsled was analyzed at 25, 40, and 55 deg. angle of attack to assess the impact on radiative heat flux. The resulting distributions along the centerline of the ellipsled are shown in Figure 19. For reference, the stagnation point radiative heat flux is about 8.6 W/cm^2 for all cases studied. Figures 20 and

21 provide additional context for the radiative heating environment by presenting contours of flowfield temperatures in the symmetry plane and at the X/L = 0.9 axial station, respectively. Contours of translational temperature are represented by colored fill, while two levels of relative vibrational temperature (+10% and -10%) indicate regions of thermodynamic nonequilibrium.

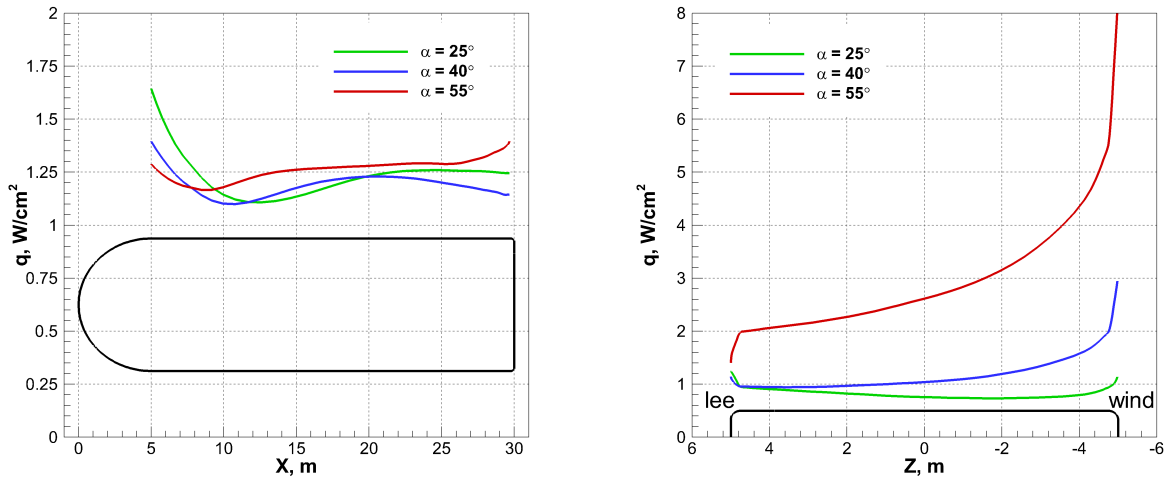

(a) Centerline. (b) Base.

Figure 19: Backshell radiation along centerline, varying angle of attack.

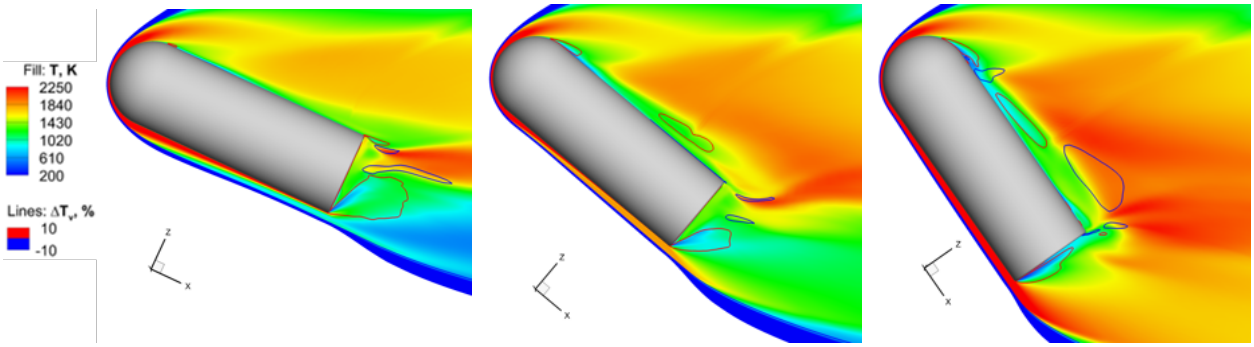

(a) 25 deg. (b) 40 deg. (c) 55 deg.

Figure 20: Contours of translational temperature (fill) and relative vibrational temperature (lines) at symmetry plane.

Beginning at the forward portion of the leeside centerline (X = 5 m) in Figure 19(a), all distributions indicate an initial peak in radiative heat flux on the nose, where the gas had been heated by the bow shock. As the flow rapidly expands over the nose, this gas is cooled and the radiative heat flux decreases. As angle of attack increases, this initial peak and subsequent expansion moves forward on the ellipsled.

The leeside flow over the ellipsled is dominated by large regions of separated flow, at all angles of attack. Flow rapidly expands laterally around the sides of the ellipsled onto the leeside surface and eventually separates and rolls up into counter-rotating helical vortices. These vortices form a region of cooler gas along the ellipsled leeside surface (see Figure 20). The size of this vortex region thus impacts the extent of reduction seen in the radiative heat flux. As angle of attack increases, the separation point for these vortices moves forward along the ellipsled leeside surface, increasing their axial coverage, however eventually interaction with base flow can cause these vortices to separate axially near the end of the leeside body. Opposing the cooling effect of the vortices is a large region of compressed and heated gas located near the afterbody flow field symmetry plane. Flow that has expanded axially over the nose is deflected upward away from the leeside surface by the vortex flow, potentially forming a shock that emanates from the point of separation. The

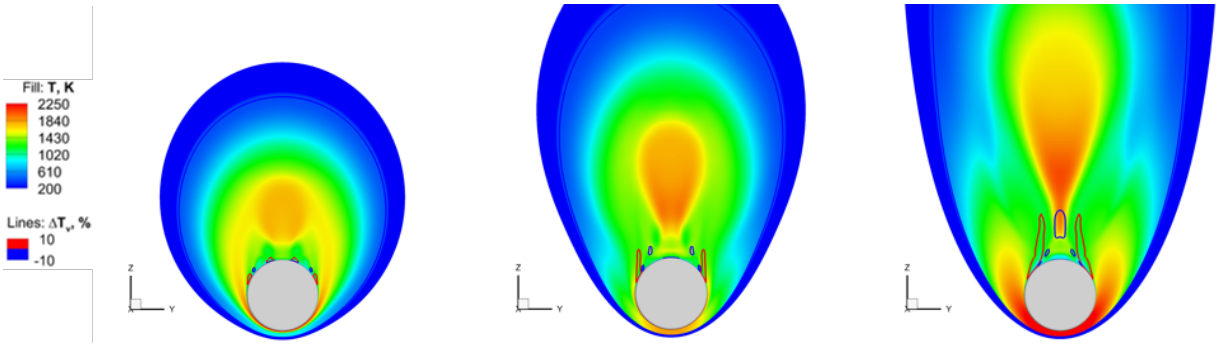

(a) 25 deg. (b) 40 deg. (c) 55 deg.

Figure 21: Contours of translational temperature (fill) and relative vibrational temperature (lines) at X/L = 0.9 axial plane.

rapid compression results in heated gas flowing over the leeside vortices (see Figure 20). Because the point of axial separation moves forward with increasing angle of attack, this region of deflected, high-temperature gas also moves forward with increasing angle of attack. This region of the flow field increases the incident radiation, as shown in the axial heat flux distributions along the leeside centerline (Figure 19(a)). The heat flux, initially decreasing due to the cooling of expanding gases, now increases due to exposure to hotter gases in the afterbody flow field.

Flow that has expanded laterally around the body must eventually be returned parallel with the symmetry plane because, at least in terms of the current computational model, this flow cannot penetrate the symmetry plane. This turning results in compression and an attendant increase in flowfield temperature (see Figure 21). The result is an increase in radiative heat transfer to the body. As angle of attack increases, the magnitude of flow velocity in the transverse direction around the ellipsled increases. Therefore, the compression and attendant temperature rise is also increased at the afterbody flowfield symmetry plane. This progression in the flowfield is evident in Figure 21.

The trade-off between higher temperatures in the afterbody flow field symmetry plane and lower temperatures within the vortices determines whether or not the distribution in radiative heat flux will increase or decrease axially along the ellipsled backshell. However, given the significant changes in the flow field that occur with changing angle of attack, there is little change to the overall magnitude in the radiation along the leeside centerline. The small differences that are observed are likely in the noise of the uncertainty in the modeling approach.

The distributions in radiative heat flux along the centerline of the base are greatly influenced by changes angle of attack (see Figure 19(b)). At an angle of attack of 25 deg., the heat flux initially decreases moving from the leeside corner toward the windside corner of the base, further away from the compressed, high-temperature gas at the wake neck. At the windside corner, flow has rapidly expanded from the forebody shock layer into the base region. At this low angle of attack, the flow turning angle into the base region is very large and the translational temperature drops significantly; however, this rapidly expanding flow is in thermodynamic nonequilibrium and the vibrational temperature remains high well into the base region (see Figure 20(a)). This higher vibrational energy ultimately causes radiative heat flux to increase as the windside corner of the base is approached along the centerline. This trend is similar to what was observed for the sphere-cone leeside shoulder. The excited flow from the forebody rapidly expands around the shoulder, which leads to a region of flow that has not yet equilibrated.

As angle of attack is increased to 40 deg., the radiative heat flux decreases in the immediate vicinity of the leeside corner of the base, moving away from compressed, high-temperature wake flow. Otherwise, in moving from the leeside corner to the windside corner of the base, the heat flux exhibits a gradual increase. While some rapid, nonequilibrium expansion persists at the windside corner at this angle of attack (see Figure 20(b)), a bigger impact to the radiation is the stronger bow shock and the corresponding higher shock-layer temperature. As this high-temperature shock layer extends beyond the full length of the ellipsled, excited CO_2 is able to radiate toward the base.

The behavior is similar as angle of attack is increased to 55 deg. However, in this case the radiative heat flux increases along the entire length of the base centerline, precipitously so as the windside corner of the

base is approached. The chief cause of this rise is again an increase in bow shock strength and shock-layer temperatures (relative to the 25 deg. case). At this increased angle of attack, the base of the ellipsled is exposed to an even larger volume of high-temperature gas. Similar to the 40 deg. case, a large rise in radiative heat flux occurs on the windside shoulder itself.

B. Ellipsled Length Dependency

At a fixed 40 deg. angle of attack, ellipsled configurations with lengths of 20, 30, and 40 m were analyzed to assess the impact of varying length on the backshell radiative heat flux. The resulting distributions along the centerline of the ellipsled are shown in Figure 22. Figures 7 provides context for the radiative heating environment by presenting contours of flowfield temperatures in the symmetry plane. Contours of translational temperature are represented by colored fill, while two levels of relative vibrational temperature (+10% and -10%) indicate regions of thermodynamic nonequilibrium.

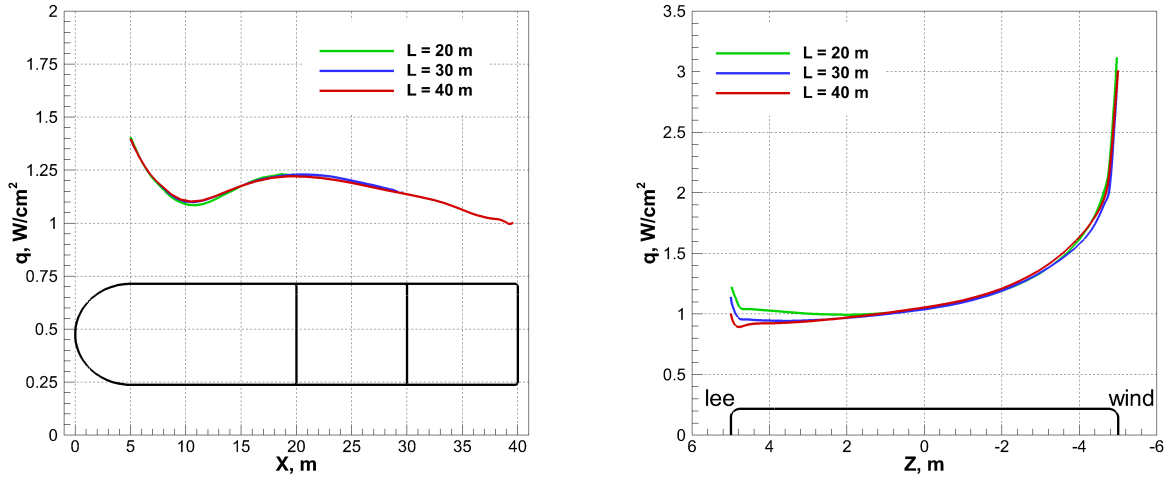

(a) Centerline. (b) Base.

Figure 22: Backshell radiation along centerline, varying ellipsled length.

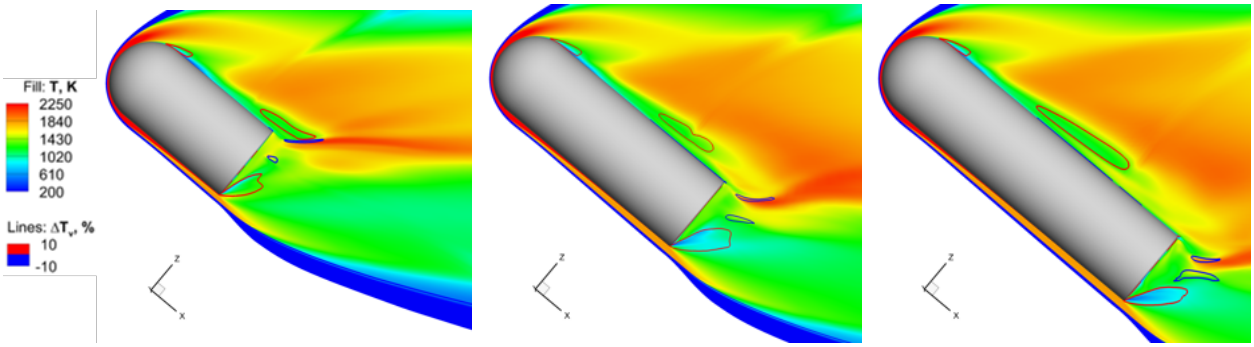

(a) 20 m. (b) 30 m. (c) 40 m.

Figure 23: Contours of translational temperature (fill) and relative vibrational temperature (lines) at symmetry plane for varying length.

The overall behavior in the radiative heat flux distributions (Figure 22(a)) suggests that any impacts of increasing ellipsled length on the flow field do not feed forward and affect the distribution ahead of that added length. That is, as the ellipsled length is increased, the additional volume of gas does not appear to significantly modify the forward portion of the centerline heat flux distribution. The distributions for the various values of ellipsled length are therefore virtually coincident. Thus, the basic trends in backshell

radiative heat flux distribution explained for the length of 30 m at angle of attack of 40 deg. case apply here for all values of length. The only differences are that the distribution is either truncated (for length of 20 m) or extended (for length of 40 m) along the same existing trend.

Along the base centerline (Figure 19(b)), the radiative heat flux distributions follow nearly identical trends. Slight differences in magnitude are seen at the leeside corner because the structures in the leeside flow field depend on length. Because the angle of attack remains constant, the expansion of the shock layer into the base region and the compression seen at the wake flow are very similar and virtually independent of length. Therefore, in moving from the leeside corner to the windside corner along the base centerline, the radiative heat flux distributions are almost coincident. At the windside corner of the base, a slightly higher heat flux is encountered for the 20 m length ellipsled. Here, the shock layer flow at the windside corner has traversed through portions of the bow shock at the nose. The resulting temperatures at the windside corner remain somewhat higher and yield slightly higher shock layer radiation.

VI. Conclusions

The objective of this work was to investigate the radiative heating that human-scale vehicles may experience during entry and descent into the Martian atmosphere. This work has shown that, at entry conditions, the primary contributor to radiative heating is emission from the CO_2 IR band system and that radiation on the backshells of the various configurations can persist even at lower speeds than expected or previously studied. In comparing the sphere-cone and ellipsled vehicle configurations, the biggest difference is the expansion of the flow around the bodies. For the sphere-cone with a cylindrical payload, the rapid expansion for excited forebody gas around the shoulder of the heat shield leads to much higher radiative heating on the payload when compared to the ellipsled leeside at the peak backshell radiative heating condition observed for the sphere-cone entry trajectory. Geometrically, the flow has time to basically equilibrate before reaching the afterbody region, which results in lower heating. However, the same impact of the rapid expansion was observed on the base of the ellipsled where the radiative heating could be more than twice that observed for the sphere-cone, depending on the angle of attack.

Overall, this study sheds light on the potential magnitudes of baskshell, radiative heating that various configurations may experience. These results may serve to inform entry vehicle and TPS design considerations necessary to accommodate thermal radiation levels. Future work will focus on development of engineering relationships for conceptual design, mitigation of the rapid flow expansion and analyzing a wider range of conditions for the ellipsled to fully characterize the radiative environment on the backshell.

References

[1]Brune, A. J., West IV, T. K., and Hosder, S., "Comprehensive Uncertianty Analysis of Mars Entry Flows Over Hypersonic Inflatable Atmospheric Decelerators," June 2014.

[2]West IV, T. K. and Hosder, S., "Uncertainty Quantification of Hypersonic Reentry Flows with Sparse Sampling and Stochastic Expansions," *Journal of Spacecraft and Rockets*, Vol. 52, No. 1, 2015, pp. 120–133.

[3]Johnston, C. O., Brandis, A. M., , and Sutton, K., "Shock Layer Radiation Modeling and Uncertainty for Mars Entry, AIAA 2012-2866," 43^{rd} *AIAA Thermophysics Conference*, New Orleans, LA, June 2012.

[4]Johnston, C. O. and Brandis, A. M., "Modeling of nonequilibrium CO Fourth-Positive and CN Violet emission in CO_2 - N_2 gases," *Journal of Quantitative Spectroscopy and Radiative Transfer*, Vol. 149, No. 1, 2014, pp. 303–317.

[5]Johnston, C. O. and Brandis, A. M., "Feature of Afterbody Radiative Heating for Earth Entry," *Journal of Spacecraft and Rockets*, Vol. 52, No. 1, 2015, pp. 105–119.

[6]Cruden, B. A., Prabhu, D. K., and Brandis, A. M., "Measurement and Characterization of Mid-wave Infrared Radiation in CO_2 Shocks," AIAA Paper 2014-2962, June 2014.

[7]Brandis, A. M., Saunders, D. A., Johnston, C. O., Cruden, B. A., and White, T. R., "Radiative Heating on the After-Body of Martian Entry Vehicles," AIAA Paper 2015-3111, Jan. 2015.

[8]Mazaheri, A., Gnoffo, P. A., Johnston, C. O., and Kleb, B., "LAURA Users Manual: 5.4-54166," Tech. rep., NASA/TM-2011-217092, May 2009.

[9]Gnoffo, P. A., Gupta, R. N., and Shinn, J. L., "Conservation Equations and Physical Models for Hypersonic Air Flows in Thermal and Chemical Nonequilibrium," Tech. rep., NASA TP 2867, Feb. 1989.

[10]Park, C., Howe, J. T., Jaffe, R. L., and Candle, G. V., "Review of Chemical-Kinetic Problems for Future NASA Missions, II: Mars Entries," *Journal of Thermophysics and Heat Transfer*, Vol. 8, No. 1, 1994, pp. 9–23.

[11]Johnson, C. O., Hollis, B. R., and Sutton, K., "Spectrum Modeling for Air Shock-layer Radiation at Lunar-Return Conditions," *Journal of Spacecraft and Rockets*, Vol. 45, No. 5, 2008, pp. 865–878.

[12]Johnson, C. O., Hollis, B. R., and Sutton, K., "Non-Boltzman Modeling for Air Shock Layers at Lunar Return Conditions," *Journal of Spacecraft and Rockets*, Vol. 45, No. 5, 2008, pp. 879–890.

[13]Ralchenko, Y., "NIST Atomic Spectra Database, Version 3.1.0," .

[14]The Opacity Project Team, *The Opacity Project*, Vol. 1, 1995.

[15]Cunto, W., Mendoza, C., Ochsenbein, F., and Zeippen, C., "TOPbase at the CDS," *Astronomy and Astrophysics*, Vol. 275, 1993, pp. L5–L8.

[16]Mazaheri, A., Johnston, C. O., and Sefidbakht, S., "Three-Dimensional Radiation Ray-Tracing for Shock-Layer Radiative Heating Simulations," *Journal of Spacecraft and Rockets*, Vol. 50, No. 3, 2013, pp. 485–493.

[17]West IV, T. K., Hosder, S., and Johnston, C. O., "Multi-Step Uncertainty Quantification Approach Applied to Hypersonic Reentry Flows," *Journal of Spacecraft and Rockets*, Vol. 51, No. 1, 2014, pp. 296–310.

[18]Eldred, M. S., "Recent Advances in Non-Intrusive Polynomial Chaos and Stochastic Collocation Methods for Uncertainty Analysis and Design, AIAA 2009-2274," 50^{th} *AIAA/ASME/ASCE/AHS/ASC Structures*, Palm Springs, CA, May 2009.

[19]Hosder, S., Walters, R. W., and Balch, M., "Point-Collocation Nonintrusive Polynomial Chaos Method for Stochastic Computational Fluid Dynamics," *AIAA Journal*, Vol. 48, No. 12, 2010, pp. 2721–2730.

[20]West IV, T. K., Brune, A. J., Hosder, S., and Johnstons, C. O., "Uncertainty Analysis of Radiative Heating Predictions for Titan Entry," *Journal of Thermophysics and Heat Transfer*, 2015.

[21]Sudret, B., "Global sensitivity analysis using polynomial chaos expansion," *Reliability Engineering and System Safety*, Vol. 93, No. 7, 2008, pp. 964–979.

[22]Hughes, S. J., Cheatwood, F. M., Dillman, R. A., Wright, H. S., DelCorso, J. A., and Calomino, A. M., "Hypersonic Inflatable Aerodynamic Decelerator (HIAD) Technology Development Overview," 21^{st} *AIAA Aerodynamic Decelerator Systems Technology conference and Seminar*, AIAA Paper 2011-2524, Dublin, Ireland, May 2011.

[23]Drake, B. G., "Human Exploration of Mars: Design Reference Architecture 5.0," Tech. Rep. NASA SP-2009-566, July 2009.

[24]Dwyer Cianciolo, A. D. and et al., "Entry, Descent, and Landing Systems Analysis Study: Phase 1 Report," Tech. Rep. NASA TM-2010-216720, July 2010.